Synthesis of Hierarchical Layered Quasi-Triangular Ce(OH)CO₃ and Its Thermal Conversion to Ceria with High Polishing Performance

Jing Li,* Rucheng He, Guihua Guo, Yao Li, Yuanyuan Liao, and Yongxiu Li*

ACCESS | Metrics & More | Article Recommendations | SI Supporting Information

ABSTRACT: Layered quasi-triangular $Ce(OH)CO_3$ assembled from primary nanoparticles was synthesized via a solvothermal method and converted into CeO_2 abrasive particles by calcination at 800−1000 °C. With the increase of calcination temperature, the primary particle size increased and the microstructure, mechanical hardness, and chemical activity of the CeO_2 particles changed, thus affecting the polishing performance. The calcined products obtained at 800, 850, and 900 °C maintained the layered edge structure of the $Ce(OH)CO_3$ precursor and had a relatively high specific surface area and surface Ce^{3+} concentration. The samples calcined at 950 and 1000 °C lost the layered structure due to the large-scale melting of the primary particles, and their surface chemical activity decreased. The polishing experiments on K9 glass showed that, with the calcination temperature rising from 800 to 1000 °C, the material removal rate (MRR) first increased and then decreased sharply. The initial increase of MRR was attributed to the increase of mechanical hardness of the layered quasi-triangular CeO_2, and the subsequent decrease of MRR was related to the decrease in surface chemical activity and disappearance of the layered edge structure. The product calcined at 900 °C had the highest MRR and best surface quality after polishing due to the layered edge structure and optimal match of chemical activity and mechanical hardness.
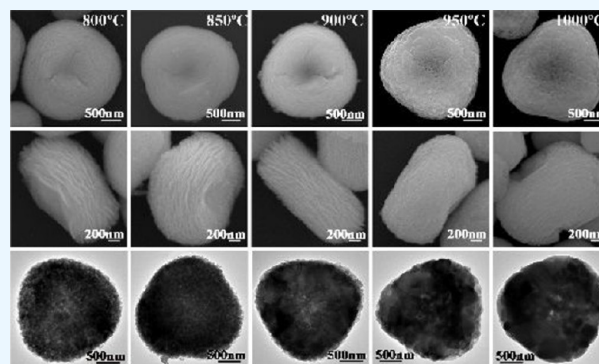
1. INTRODUCTION

The controlled synthesis of rare-earth architectures with different geometries has been of great importance because their optical, electric, magnetic, and catalytic properties are highly dependent on the size and shape of the particles.[1−4] Ceria, one of the promising rare-earth oxide functional materials, is of great interest due to its high mobility of oxygen vacancies, reversible redox transformation between Ce^{4+} and Ce^{3+}, and applications in catalysis,[5−8] polishing materials,[9−11] and electrolyte materials for solid oxide fuel cells (SOFCs).[12−14] Extensive studies have been carried out with respect to the size and shape control of cubic-fluorite-structured ceria. A number of CeO_2 architectures with various morphologies have been successfully fabricated, including nanocubes with {100} faces,[15−17] nano-octahedra with {111} surfaces,[18−20] and nanorods with exposed {110} and {100} planes[17,21−23] as well as hierarchical organizations of octahedra,[24,25] spheres,[26−28] flowers,[29−31] and urchin-like structures.[32]

Ceria particles with different sizes/morphologies/structures usually exhibit different application properties. For example, CeO_2 particles with a hierarchical structure showed enhanced catalytic activity due to their high surface area and unique microstructure. The catalytic activity of hierarchical CeO_2 octahedra assembled from primary nanoparticles for CO oxidation was higher than that of single-crystal octahedra of the same size.[24] Flowerlike hierarchical CeO_2 spheres exhibited much higher catalytic activity than general CeO_2 particles for the combustion of trichloroethylene.[27]

As a polishing material, ceria has also exhibited size-/morphology-/structure-dependent polishing properties. In glass polishing, nanosized ceria particles mainly achieved material removal through a chemical reaction, while microsized ceria abrasive underwent both a chemical reaction and mechanical friction.[33] CeO_2 nanoparticles with a mixed morphology of rods and cubes exhibited a better surface finish and the highest material removal rate (MRR) in glass polishing compared with nanocubes and nanospheres.[34] CeO_2 nano-octahedra with {111} facets had a higher MRR for single-crystal silicon than nanospheres because the abrasion mechanism of the silicon substrate polished by the nano-octahedra with sharp edges and corners was microploughing wear, while that polished by nanospheres was microscale abrasive wear.[35] Compared with single-crystal hexagonal
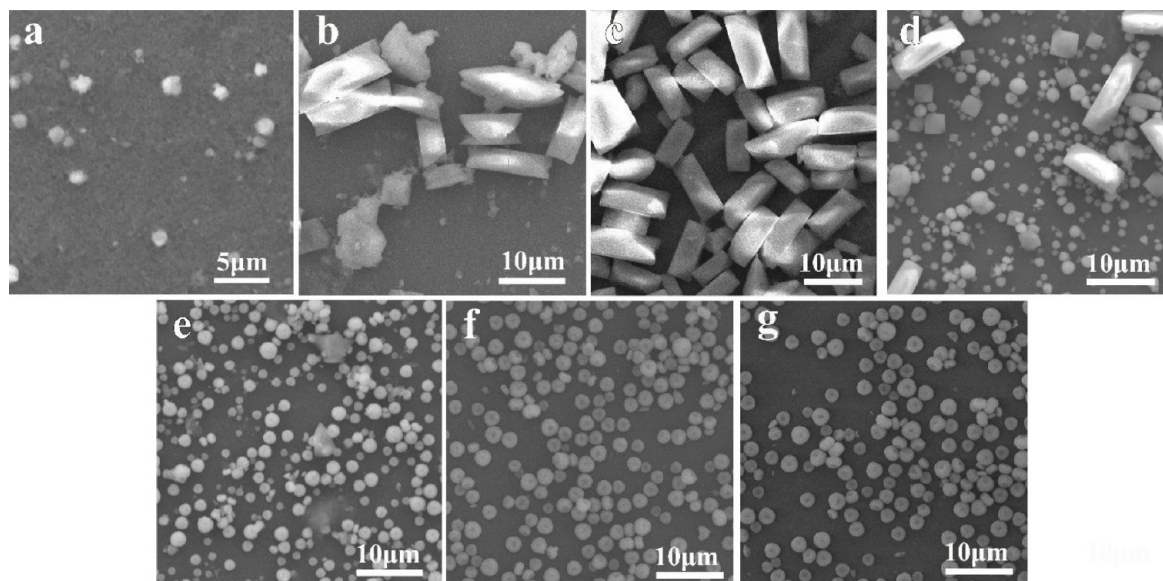
Figure 1. SEM images of the samples obtained at 180 °C for solvothermal times of 4 h (a), 8 h (b), 12 h (c), 16 h (d), 20 h (e), 24 h (f), and 36 h (g).

particles, hierarchical nanospheres of CeO_2 exhibited a superior removal rate and scratch suppression ability in chemical−mechanical polishing (CMP) of a SiO_2 wafer due to their physical softness and high chemical activity.[36]

Although the effect of the ceria abrasive morphology on its mechanical and chemical polishing properties has been investigated, the studies were focused on simple-structured particles. Ceria particles with a hierarchical structure are fascinating because their complicated spatial arrangement may give rise to enhanced chemophysical properties and polishing performance. In this paper, a hierarchical layered quasi-triangular $Ce(OH)CO_3$ precursor was synthesized by a solvothermal reaction and then converted to hierarchical quasi-triangular CeO_2 particles with different microstructures by calcination at different temperatures. The formation mechanism of the precursor and the correlation between the microstructure of hierarchical quasi-triangular CeO_2 and its polishing performance are discussed.

2. EXPERIMENTAL SECTION

2.1. Preparation. All chemicals were of analytical grade and were used without further purification. The water used in the experiments was deionized (DI) water. Typically, 6.52 g of $Ce(NO_3)_3 \cdot 6H_2O$ and 12.0 g of polyvinylpyrrolidone (PVP, K30) were dissolved in 250 mL of ethylene glycol (EG). Then, 50 mL of 0.3 M ammonia aqueous solution was added dropwise into the above mixture with stirring. After further stirring for 30 min, the resulting solution (pH ≈ 7.3) was transferred into a Teflon-lined stainless steel autoclave (capacity 500 mL) and heated at 180 °C for 4, 8, 12, 16, 20, 24, or 36 h. After the autoclave cooled to room temperature, the precipitate was separated by centrifugation, washed with DI water and ethanol, and dried at 50 °C for 12 h. The precursor synthesized with a reaction time of 24 h was put into an alumina crucible and calcined in a muffle furnace under an air atmosphere at various temperatures from 800 to 1000 °C for 3 h at a heating rate of 10 °C/min. After calcining, the samples were cooled to room temperature in the furnace.

2.2. Characterization. The composition and phase of the samples were characterized using X-ray powder diffraction (XRD) on a Bruker axs D8 Advance X-ray diffractometer with Cu Kα radiation (λ = 0.15406 nm). The morphology and crystal structure were examined using scanning electron microscopy (SEM) with a FEI Quanta-200F microscope operated at an acceleration voltage of 20 kV and transmission electron microscopy (TEM) on a JEOL JEM-2100 microscope operated at 200 kV. Thermogravimetric (TG) analysis was performed on a PerkinElmer TGA 4000 instrument to monitor the mass loss of the sample as a function of temperature from room temperature to 800 °C at a heating rate of 10 °C/min under an air atmosphere. The specific surface area of the calcined samples was measured using the BET method (N_2 adsorption) with a Quantachrome Autosorb-iQ gas adsorption analyzer. The surface ζ potential measurement of ceria abrasive was performed using an Agilent Zetaprobe 7020 instrument. The surface cerium valence states of the calcined products were detected using X-ray photoelectron spectroscopy (XPS) on a Thermo Scientific Escalab 250Xi with Al Kα radiation ($h\nu$ = 1486.6 eV).

2.3. Polishing Tests. The slurry was prepared by dispersing ceria abrasive obtained at different calcination temperatures in DI water with stirring and then treated by ultrasound for 15 min. The concentration of ceria abrasive was 5.0 wt %. The pH value of the slurry was about 6.6. CMP tests were performed at K9 optical glass wafers with a diameter of 6.0 cm and a thickness of 2.0 mm with a UNIPOL-802 polishing machine (Shenyang Kejing Co. Ltd.) equipped with a slurry circulation system. The polishing process parameters were set as follows: use of a synthetic leather polishing pad, pad rotation speed 200 rpm, down pressure 6.6 kPa, feed rate of the slurry 2 L/min, polishing temperature 25 ± 2 °C, and polishing time 1 h. After polishing, the wafers were rinsed with absolute ethyl alcohol and DI water and then dried naturally in a superclean room. The material removal rate (MRR) was calculated by MRR = $(m_0 - m)/\rho t S$, where ρ is the density of K9 glass (2.51 g/cm^3), S is the area of the wafer, t is the polishing time, m_0 is the original mass of the wafer, and m is
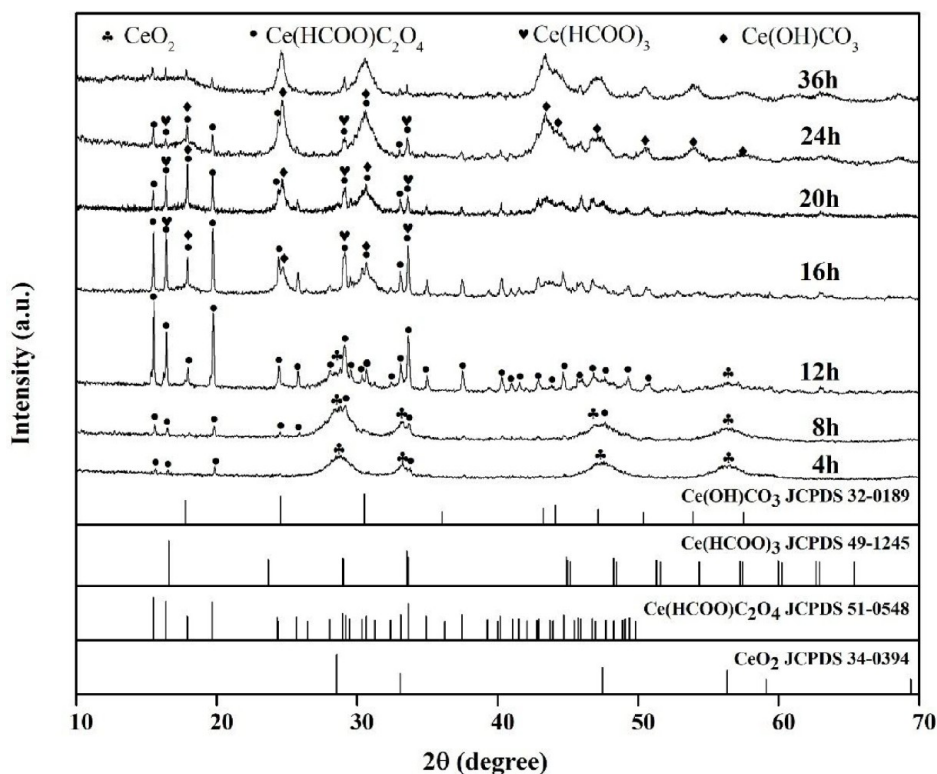
Figure 2. XRD patterns of the samples obtained at 180 °C for solvothermal times of 4, 8, 12, 16, 20, 24, and 36 h.
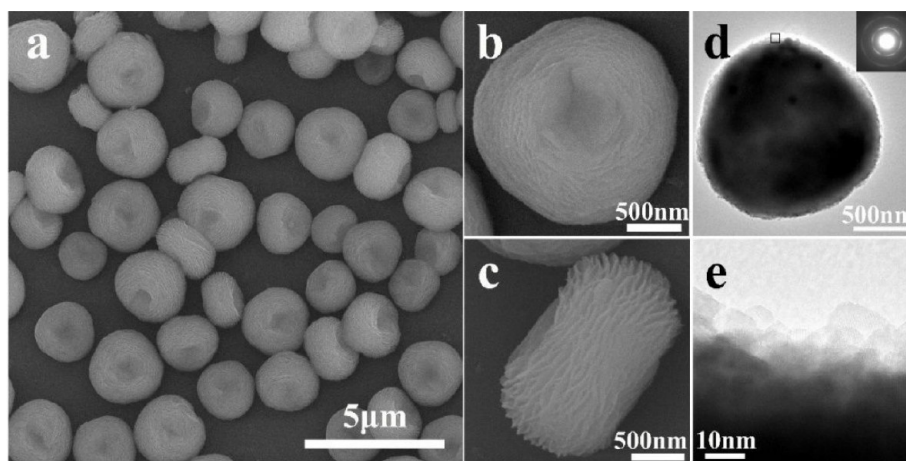

Figure 3. (a–c) High-magnification SEM images of the sample synthesized at 180 °C for a solvothermal time of 24 h, showing its concave layered quasi-triangular structure. (d) TEM image of a single particle and corresponding SAED pattern (inset). (e) HRTEM image recorded from the black-box region marked in d.

the mass of the wafer after polishing. A Sartorius precision electron balance was used to measure the mass of K9 glass (before and after polishing), and all the MRR values were the average of three measurements. The topography of the K9 surface was measured with a SuperView W1 surface profilometer (Chotest Technology Inc.).

3. RESULTS AND DISCUSSION

3.1. Hierarchical Layered Quasi-Triangular Precursor and Its Formation Mechanism. The solvothermal reaction time has a significant influence on the morphology and phase of the precursors. As shown in Figures 1 and 2, when the reaction time was 4 h, the main product was nanosized small particles accompanied by some large particles. The corre-

sponding XRD pattern showed that the phase composition of the sample was cubic fluorite CeO_2 (JCPDS 34-0394) along with a trace amount of orthorhombic $Ce(HCOO)C_2O_4$ (JCPDS 51-0548). As the solvothermal time was extended to 8 h, micrometer-sized rods were formed and they became the main product at the solvothermal time of 12 h. Correspondingly, the intensity of the characteristic diffraction peaks of orthorhombic $Ce(HCOO)C_2O_4$ increased significantly. The position and intensity of the main diffraction peaks of the sample after a solvothermal reaction for 12 h were in good agreement with the standard data of JCPDS 51-0548, indicating that the rod-shaped particles were the $Ce(HCOO)$-C_2O_4 phase. But there were still two weak diffraction peaks at $2\theta = 28.5$ and $56.3°$, which belong to CeO_2 phase diffraction.
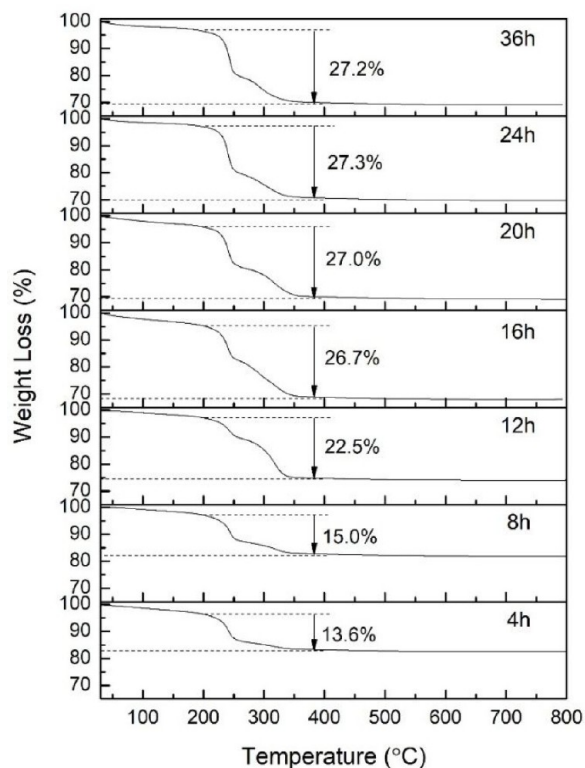
Figure 4. TG curves of the samples obtained at 180 °C for solvothermal times of 4, 8, 12, 16, 20, 24, and 36 h.

When the reaction time reached 16 h, quasi-triangular particles emerged in the product. Accordingly, the intensity of diffraction peaks at 2θ = 15.5 and 19.7° ascribed to $Ce(HCOO)C_2O_4$ decreased. At the same time, the relative intensity of diffraction peaks at 2θ = 16.5, 17.9, and 30.6° increased and a new peak appeared at 2θ = 24.6°. The increase in the relative intensity of the diffraction peak at 2θ = 16.5° was attributed to the newly formed hexagonal phase of
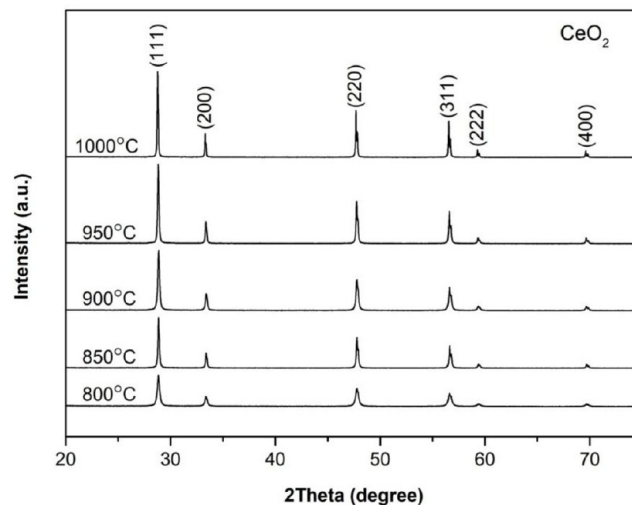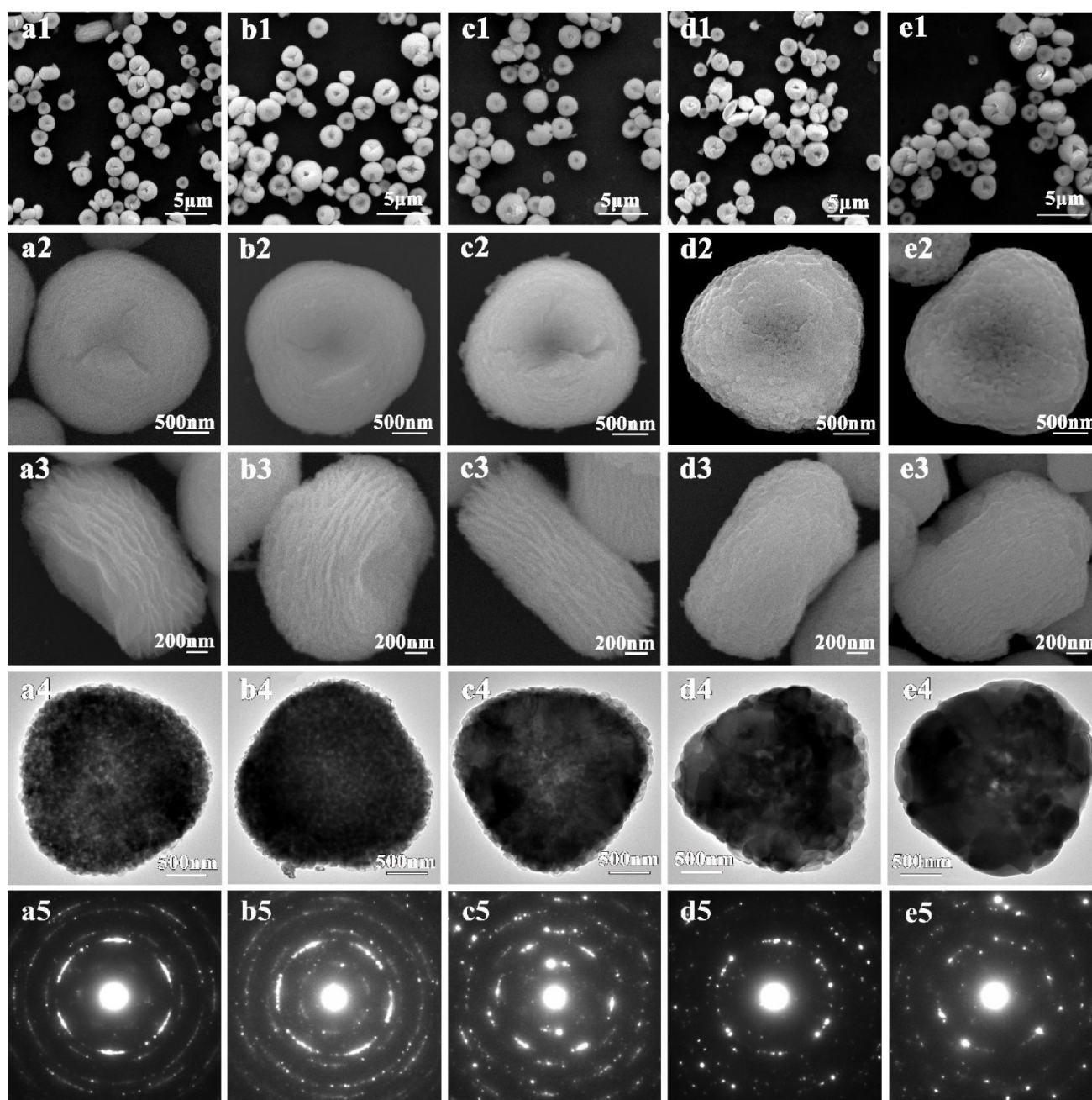

Figure 6. XRD patterns of the products obtained by calcining the layered quasi-triangular precursor in air at 800, 850, 900, 950, and 1000 °C for 3 h.

$Ce(HCOO)_3$ (JCPDS 49-1245), whose characteristic diffraction peaks at 2θ = 16.5, 29.1, and 33.6° overlapped with those of the previously formed $Ce(HCOO)C_2O_4$. Simultaneously, the newly formed hexagonal phase of $Ce(OH)CO_3$ (JCPDS 32-0189) led to an increment of diffraction peak intensity at 2θ = 17.9 and 30.6° as well as a new peak at 2θ = 24.6°. No obvious CeO_2 diffraction peak was observed in the XRD pattern of this sample. After 20 h of solvothermal reaction, quasi-triangular particles were dominant in the product, but there were still a certain number of residual fragments of the previously formed rods. The XRD characterization indicated that the sample was composed of $Ce(OH)CO_3$, $Ce(HCOO)_3$, and $Ce(HCOO)C_2O_4$ phases. Compared with the product reacted for 16 h, the characteristic diffraction peak intensity of $Ce(HCOO)C_2O_4$ and $Ce(HCOO)_3$ decreased while that of $Ce(OH)CO_3$ increased. When the solvothermal time was
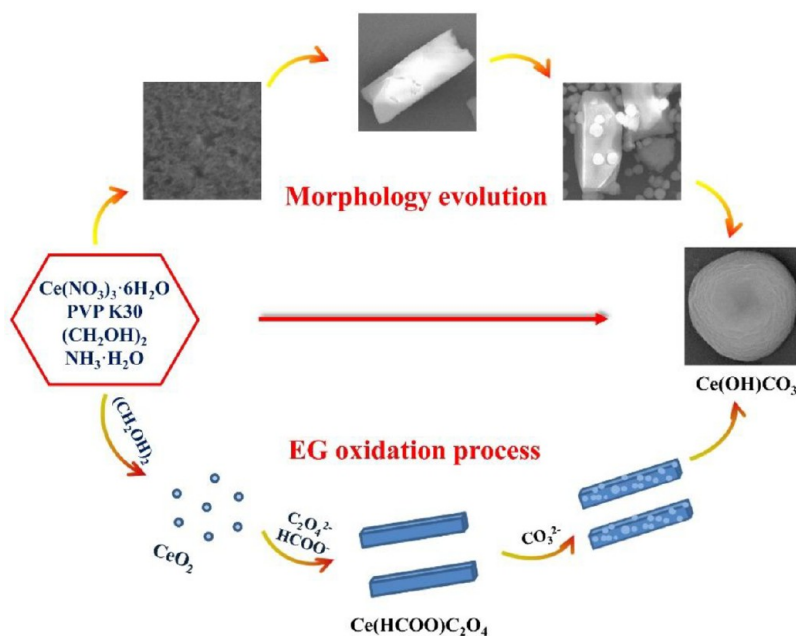
Figure 5. Schematic illustration of the mechanism responsible for the formation of the hierarchical layered quasi-triangular precursor.

Figure 7. SEM images of the products obtained by calcining the layered quasi-triangular precursor in air at 800 (a1), 850 (b1), 900 (c1), 950 (d1), and 1000 °C (e1) for 3 h. High-magnification SEM images of a single particle with different orientations obtained at calcination temperatures of 800 (a2, a3), 850 (b2, b3), 900 (c2, c3), 950 (d2, d3), and 1000 °C (e2, e3). TEM images of a single calcined particle and corresponding SAED patterns: (a4, a5) 800 °C; (b4, b5) 850 °C; (c4, c5) 900 °C; (d4, d5) 950 °C; (e4, e5) 1000 °C.

Table 1. Specific Surface Area, ζ Potential, and Surface Ce^{3+} Concentration of the Calcined Products

| calcination temp (°C)	specific surface area (m²/g)	ζ potential (mV)	surface Ce^{3+} concn (%)
800	13.30	36.7	23.65
850	10.55	38.0	23.17
900	10.45	39.4	23.67
950	6.93	34.2	21.60
1000	4.07	15.3	21.49

extended to 24 h, quasi-triangular particles with a uniform size became the main product and further extension of the reaction time to 36 h had little effect on the morphology of the product.

An XRD analysis demonstrated that the samples reacted for 24 and 36 h were mainly the $Ce(OH)CO_3$ phase with a small amount of $Ce(HCOO)C_2O_4$ and $Ce(HCOO)_3$ phases.

High-magnification SEM images of the quasi-triangular particles synthesized at 180 °C for a solvothermal time of 24 h revealed that they had a concave center and layered edges (Figure 3a−c). The particle size ranged from 1.2 to 2.8 μm. The structure was further studied using TEM, selected area electron diffraction (SAED), and high-resolution TEM (HRTEM). As shown in Figure 3d,e, the concave layered quasi-triangular particle possessed a hierarchical structure which was formed through the aggregation of small primary nanoparticles. SAED showed a symmetrical arc-like pattern,
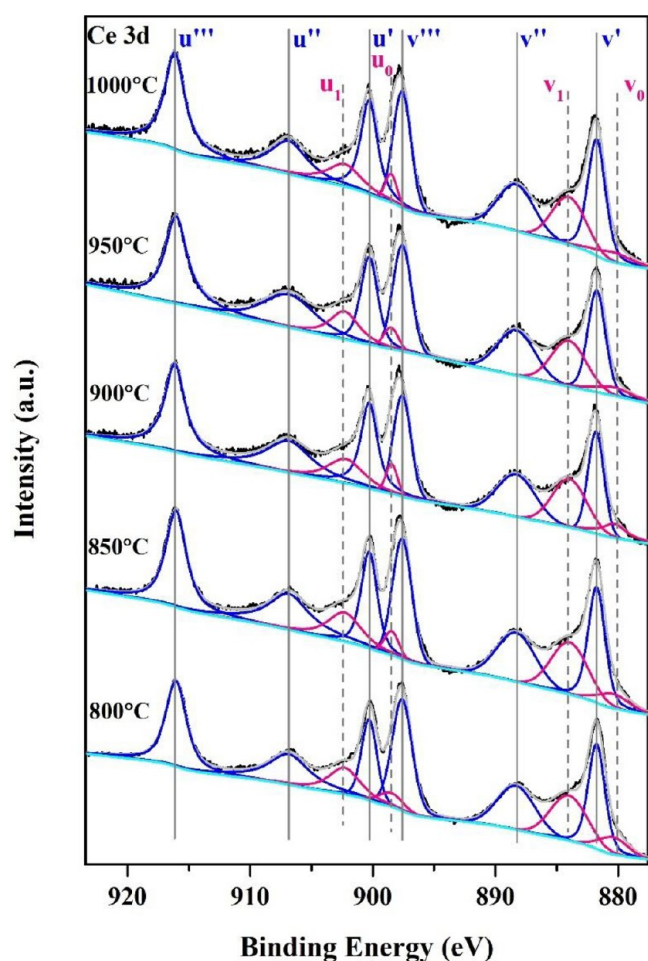
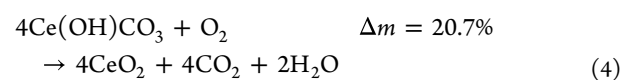**Figure 8.** Ce 3d XPS spectra for the products calcined at different temperatures.
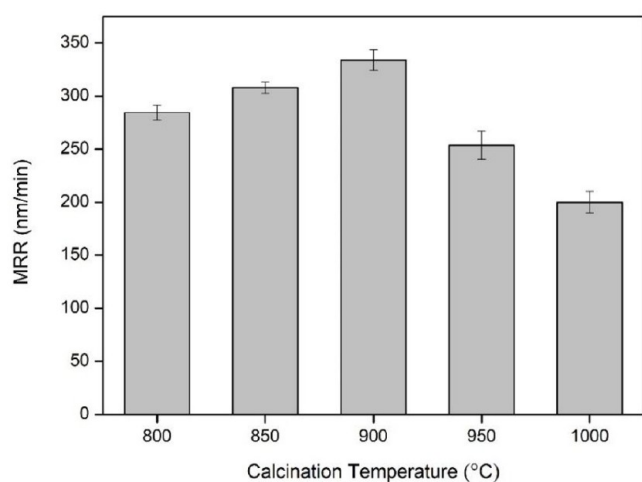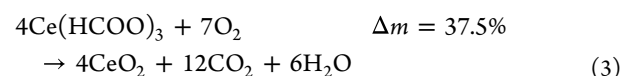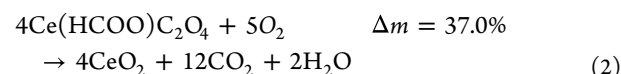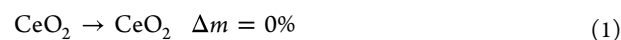

Figure 9. MRR of K9 glass by the products calcined at different temperatures.

indicating that the primary nanoparticles were aggregated with large-angle misorientation.[37,38]
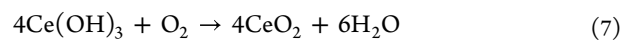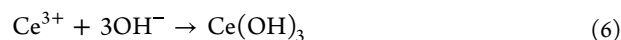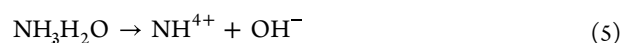
The thermal behavior of the samples for different solvothermal reaction time was investigated with TG. As shown in Figure 4, the weight loss before 200 °C was attributed to the removal of free water or adsorbed water, while the significant weight loss from 200 to 400 °C was attributed
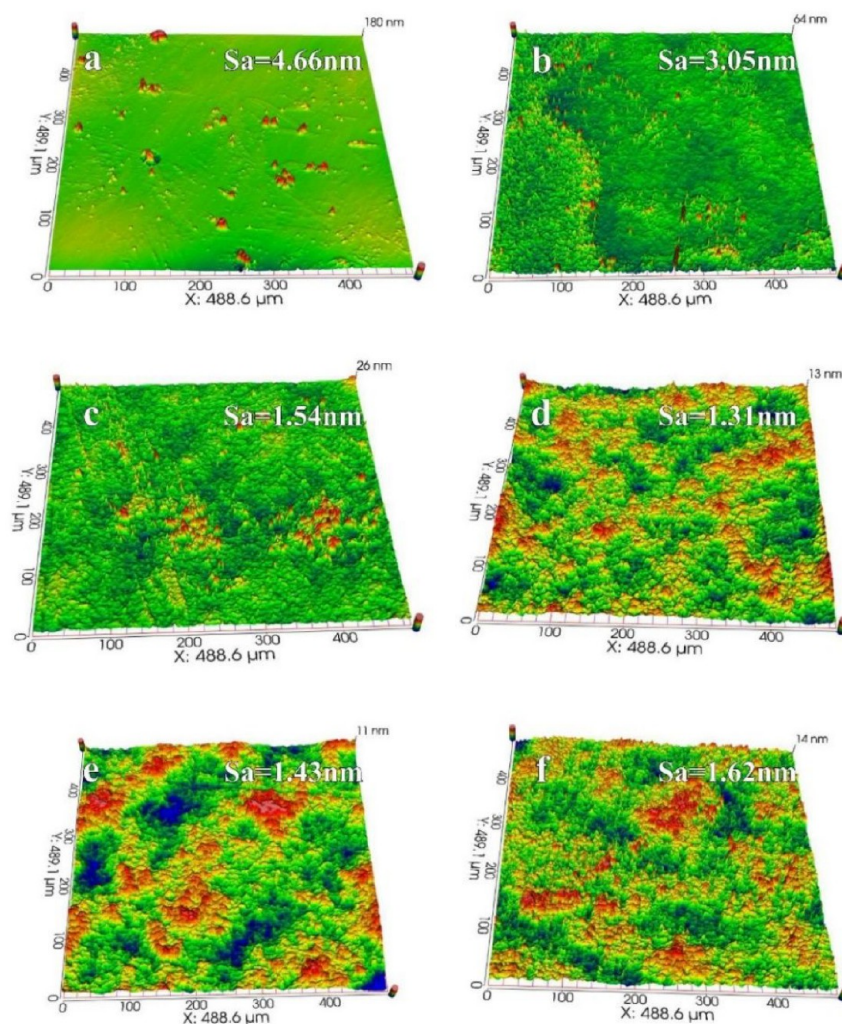
to the decomposition of the mixed-phase cerium compound samples.[39,40] The total weight loss between 200 and 400 °C first increased and then remained basically unchanged with an extension of the reaction time, corresponding to the transformation of the dominant phase of the product from CeO_2 to $Ce(HCOO)C_2O_4$, $Ce(HCOO)_3$, and $Ce(OH)CO_3$. The theoretical weight loss values of CeO_2, $Ce(HCOO)C_2O_4$, $Ce(HCOO)_3$ and $Ce(OH)CO_3$ can be calculated from the following reactions:[41]

$$CeO_2 \rightarrow CeO_2 \quad \Delta m = 0\% \tag{1}$$

$$4Ce(HCOO)C_2O_4 + 5O_2 \quad \Delta m = 37.0\%$$
$$\rightarrow 4CeO_2 + 12CO_2 + 2H_2O \tag{2}$$

$$4Ce(HCOO)_3 + 7O_2 \quad \Delta m = 37.5\%$$
$$\rightarrow 4CeO_2 + 12CO_2 + 6H_2O \tag{3}$$

$$4Ce(OH)CO_3 + O_2 \quad \Delta m = 20.7\%$$
$$\rightarrow 4CeO_2 + 4CO_2 + 2H_2O \tag{4}$$

During the solvothermal reaction time of 4−12 h, with the increase of the $Ce(HCOO)C_2O_4$ phase and the decrease of the CeO_2 phase in the product, the total weight loss between 200 and 400 °C increased from ~13.6% to ~22.5%. A mixed-phase product of $Ce(HCOO)C_2O_4$, $Ce(HCOO)_3$, and $Ce(OH)CO_3$ with a total weight loss of ~26.7% was obtained at a reaction time of 16 h. As the reaction time was extended from 16 to 24 h, the $Ce(OH)CO_3$ phase in the mixed-phase product increased, which should lead to a decrease in total weight loss, since $Ce(OH)CO_3$ has a lower theoretical weight loss value compared to $Ce(HCOO)C_2O_4$ and $Ce(HCOO)_3$. However, the weight loss of the sample reacted for 24 h was slightly greater than that of the sample reacted for 16 h. This may be due to the conversion of CeO_2 to $Ce(HCOO)C_2O_4$ or $Ce(HCOO)_3$ during the solvothermal time of 16−24 h, although no obvious CeO_2 phase was observed in the XRD pattern of these samples. When the reaction time increased from 24 to 36 h, the composition of the product remained basically unchanged, that is, a mixed-phase product dominated by the $Ce(OH)CO_3$ phase; thus, the total weight loss changed little.

The possible mechanism for the formation of the hierarchical layered quasi-triangular precursor is presented in Figure 5. The initial feeding included $Ce(NO_3)_3·6H_2O$, PVP K30, EG, and ammonia aqueous solution, and the pH value of this mixed solution was ~7.3. With an increase in the solvothermal time, the morphology of the product evolved from fine nanoparticles to micrometer-sized rods and finally to the layered quasi-triangular structure and the corresponding main phase changed from CeO_2 to $Ce(HCOO)C_2O_4$ and finally to $Ce(OH)CO_3$. The evolution of the product morphology and the main phase was related to the oxidation process of the solvent EG. The chemical reactions involved were as follows:[42−44]

$$NH_3H_2O \rightarrow NH^{4+} + OH^- \tag{5}$$

$$Ce^{3+} + 3OH^- \rightarrow Ce(OH)_3 \tag{6}$$

$$4Ce(OH)_3 + O_2 \rightarrow 4CeO_2 + 6H_2O \tag{7}$$

Figure 10. Surface topography of K9 glass before (a) and after polishing using the products calcined at 800 (b), 850 (c), 900 (d), 950 (e), and 1000 °C (f) as abrasive particles.
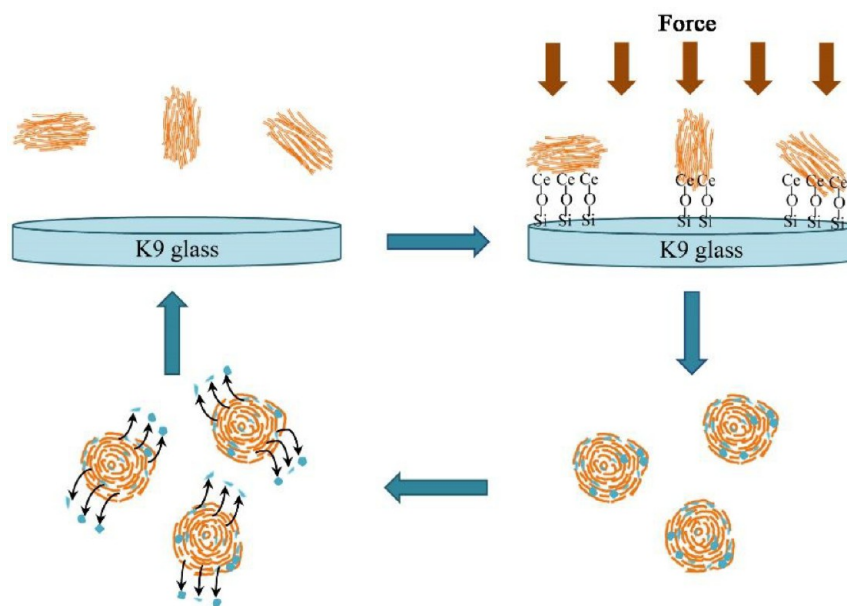
Figure 11. Schematics illustrating the polishing mechanism of the hierarchical layered quasi-triangular CeO_2.

$$8CeO_2 + (CH_2OH)_2 + 22H^+$$
$$\rightarrow 8Ce^{3+} + C_2O_4^{2-} + 14H_2O \qquad (8)$$

$$6CeO_2 + (CH_2OH)_2 + 16H^+$$
$$\rightarrow 6Ce^{3+} + 2HCOO^- + 10H_2O \qquad (9)$$

$$Ce^{3+} + HCOO^- + C_2O_4^{2-} \rightarrow Ce(HCOO)C_2O_4 \qquad (10)$$

$$2CeO_2 + C_2O_4^{2-} + 4H^+ \rightarrow 2Ce^{3+} + 2CO_3^{2-} + 2H_2O \qquad (11)$$

$$Ce^{3+} + 3HCOO^- \rightarrow Ce(HCOO)_3 \qquad (12)$$

$$Ce^{3+} + CO_3^{2-} + OH^- \rightarrow Ce(OH)CO_3 \qquad (13)$$

$$2CeO_2 + HCOO^- + 5H^+ \rightarrow 2Ce^{3+} + CO_3^{2-} + 3H_2O \qquad (14)$$
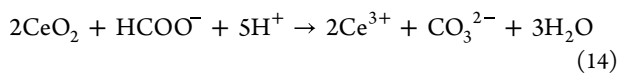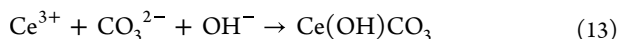
In the initial stage of solvothermal treatment, the main reaction was the oxidation of Ce^{3+} in the presence of OH^- to form CeO_2, as illustrated in reactions 5–7. Due to the insufficient amount of ammonia as precipitant (the molar ratio of Ce^{3+} to ammonia is 1:1 at the initial feeding), there was still a large amount of free Ce^{3+} in the reaction system. Under the solvothermal conditions of high temperature and high pressure, CeO_2 generated in reaction 7 oxidized the solvent EG to $C_2O_4^{2-}$ and $HCOO^-$, while itself was reduced to Ce^{3+}, as shown in reactions 8 and 9. The resulting $C_2O_4^{2-}$ and $HCOO^-$ ions then underwent precipitation (reaction 10) to form $Ce(HCOO)C_2O_4$. The continuous progress of reacti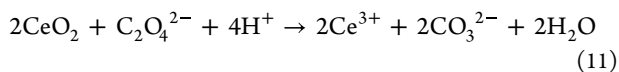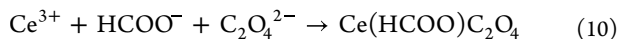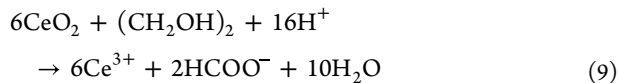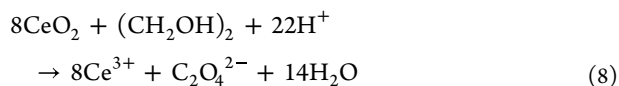ons 6–10 made $Ce(HCOO)C_2O_4$ the main phase of the product reacted for 12 h. With an extension of the solvothermal time, CeO_2 generated in reaction 7 further oxidized $C_2O_4^{2-}$ to CO_3^{2-}, as shown in reaction 11. The oxidation of $C_2O_4^{2-}$ resulted in the dissolution of $Ce(HCOO)C_2O_4$, and the released $HCOO^-$ ions combined with Ce^{3+} to produce $Ce(HCOO)_3$, as illustrated in reaction 12. Meanwhile, CO_3^{2-} ions, the oxidation product of $C_2O_4^{2-}$, reacted with Ce^{3+} and OH^- to form $Ce(OH)CO_3$, as shown in reaction 13. Thus, a mixed-phase product of $Ce(HCOO)C_2O_4$, Ce-$(HCOO)_3$, and $Ce(OH)CO_3$ was obtained at a reaction time of 16 h. Further prolongation of solvothermal time also led to the oxidation of $HCOO^-$ to CO_3^{2-} by CeO_2, as illustrated in reaction 14. The continuation of reactions 6, 7, 11, 14, and 13 made $Ce(OH)CO_3$ the dominant phase of the sample after 24 h of reaction. Owing to the continuous consumption of OH^- in reaction 13 to generate $Ce(OH)CO_3$, the acidity of the reaction system increased, which hindered the formation of CeO_2 in reactions 6 and 7. Therefore, the conversion of $Ce(HCOO)C_2O_4$ and $Ce(HCOO)_3$ to Ce-$(OH)CO_3$ was incomplete, and the product reacted for 36 h was still a mixture with $Ce(OH)CO_3$ as the main phase. A decrease in pH of the reaction system was observed with prolonged reaction time, and the pH value of the supernatant after 24 h of reaction was ~4.6. At this time, Ce^{3+} in the reaction system was basically precipitated completely. Calculated according to the weight of CeO_2 obtained by calcining the hierarchical layered quasi-triangular precursor, the yield was over 95%.

3.2. Hierarchical Quasi-Triangular CeO_2 and the CMP Performance. The hierarchical layered quasi-triangular precursor with a reaction time of 24 h was then calcined at

800–1000 °C to obtain the ceria abrasives. The XRD patterns of the calcined products are displayed in Figure 6. All of the diffraction peaks were in good agreement with JCPDS No. 34-0394, which was cubic-fluorite-structured CeO_2 with the lattice constant a = 5.41 Å. The diffraction peaks became higher and sharper with the increment of calcination temperature, indicating an improvement in crystallinity and an increase in the grain size.

The morphology and structure of the calcined products were characterized by SEM and TEM. As shown in Figure 7a1–e1, the samples calcined at different temperatures maintained a concave quasi-triangular shape. High-magnification SEM images of a single particle with different orientations showed that the samples calcined at temperatures of 800, 850, and 900 °C had layered edges similar to those of the precursor (Figure 7a2–c2,a3–c3), while for the products obtained at calcination temperatures of 950 and 1000 °C, the layered structure disappeared and the melting of the particle surface could be observed (Figure 7d2,e2,d3,e3). Further TEM characterization revealed the microstructure of the calcined products. As shown in Figure 7a4–e4, the calcined products were aggregated from primary particles. The size of the primary particles increased with the increase in calcination temperature, and the melting zone could be clearly seen for the samples calcined at 950 and 1000 °C (Figure S1). The corresponding SAED patterns are displayed in Figure 7a5–e5. The samples calcined at 800 and 850 °C showed symmetrical arc-like diffraction spots. The elongation of diffraction spots indicated that the products were aggregated from many primary particles with large-angle orientation deviations.[37,38] For the samples calcined at 900, 950, and 1000 °C, the arc-like diffraction spots gradually disappeared and individual circular diffraction spots appeared, corresponding to the melting-induced increase in primary particle size as well as a large-scale melting zone in the samples.

Table 1 shows the specific surface area, ζ potential, and surface Ce^{3+} concentration of the calcined products. As the calcination temperature increased from 800 to 900 °C, the specific surface area gradually decreased from 13.30 to 10.45 m^2/g, corresponding to the increase in primary particle size caused by the increase in calcination temperature. A further increase of calcination temperature to 950 and 1000 °C resulted in a large melting zone and disappearance of the layered structure; thus, the specific surface area dropped sharply to 6.93 and 4.07 m^2/g. The products obtained at calcination temperatures of 800–950 °C possessed ζ potential values of more than 30 mV, suggesting their good dispersion stability,[45,46] while for the product calcined at 1000 °C, its ζ potential value was 15.3 mV and the dispersion stability was poor. This may be related to the fact that the particles calcined at 1000 °C are denser due to large-area melting and the disappearance of layered edges; thus, the gravity effect is greater than that of the samples calcined at 800–950 °C. The surface Ce^{3+} concentration of the calcined products was determined from the Ce 3d XPS spectra. As shown in Figure 8, the peaks between 876.8 and 923.3 eV could be deconvoluted into ten bands, which can be divided into two multiplets, labeled as v and u, corresponding to the spin–orbit coupling of $3d_{5/2}$ and $3d_{3/2}$.[47–49] The bands denoted as v′ (u′), v″ (u″), and v‴ (u‴) can be assigned to the photoemissions from different final states of the $3d^{10}4f^0$ of Ce^{4+} ions. Meanwhile, the signals v_0 (u_0) and v_1 (u_1) are ascribed to photoemissions from different final states of $3d^{10}4f^1$ of Ce^{3+} ions. The concentration of Ce^{3+} ions in the calcined products

was calculated by dividing the area corresponding to Ce^{3+} by the total integrated area of Ce 3d (Table S1). As shown in Table 1, the surface Ce^{3+} concentrations of the products calcined at 800−1000 °C wwereas 23.65, 23.17, 23.67, 21.60, and 21.49%, respectively. The products calcined at 800, 850, and 900 °C had a higher concentration of Ce^{3+} ions than those calcined at 900 and 1000 °C, indicating their higher surface chemical activity.[50−53] Studies on the mechanism of polishing of glass and SiO_2 by CeO_2 particles have proved that ceria not only relies on mechanical friction but also reacts with the workpiece surface to achieve material removal.[54−56] In an aqueous medium, ceria and glass react with water molecules and form Ce−OH and Si−OH on the surface. During CMP, the OH groups on the ceria surface form strong Ce−O−Si bonds with Si−OH groups on the glass surface. The Ce−O−Si bonds are much stronger than Si−O−Si bonds, leading to the removal of SiO_2.[57,58] Ce^{3+} sites help the formation of Ce−OH groups at the CeO_2 surface through H_2O dissociation and facilitate the breaking up of Si−O bonds during polishing.[54−56,59,60] From the perspective of the chemical effect of CMP, the surface Ce^{3+} concentration of the products calcined at 800−900 °C is high and they should have better polishing performance.

The CMP behavior of the calcined products on K9 glass was tested. As shown in Figure 9, with the calcination temperature increasing from 800 to 1000 °C, the MRR increased first and then decreased sharply, which reflected the chemical and mechanical effects as well as microstructure factors in CMP. The samples calcined at 800−900 °C maintained the layered structure of the precursor and had similar surface Ce^{3+} concentrations. Therefore, the initial increase of MRR was attributed to the increase in mechanical hardness of the hierarchical layered quasi-triangular CeO_2 particles with an increment of calcination temperature. The products calcined at 900 °C had the highest MRR (about 333.9 nm min^{-1}). The subsequent sharp drop in MRR was ascribed to the decrease in the surface chemical activity as well as the disappearance of layered edges. The quasi-triangular CeO_2 abrasive with a layered structure has a larger specific surface area, which can provide more contact sites for a chemical reaction and mechanical friction during CMP. Moreover, the removed substances can be entrained in the layered structure and leave the workpiece surface along with the particles. Compared with the sample calcined at 950 °C, the MRR of the product calcined at 1000 °C was further reduced to about 200.0 nm min^{-1} due to its poor dispersion stability.

Figure 10 shows the surface topography of K9 glass before and after polishing with the calcined products. The roughness was measured for each sample in a 488.6 μm × 489.1 μm region. The surface roughnesses (Sa) of K9 glass after CMP with quasi-triangular CeO_2 abrasives calcined at 800, 850, 900, 950, and 1000 °C were 3.05 ± 0.13, 1.54 ± 0.09, 1.31 ± 0.06, 1.43 ± 0.07 and 1.62 ± 0.08 nm, respectively. The sample calcined at 900 °C exhibited the best surface quality after polishing. Compared with the products calcined at 850−1000 °C, the roughness of K9 glass polished by the product calcined at 800 °C was higher, which was related to the insufficient hardness of particles calcined at 800 °C. SEM characterization showed that the abrasive particles calcined at 800 °C were partially broken after polishing, while the samples calcined at 850−1000 °C had no obvious morphology change after polishing (Figure S2). For the sample calcined at 800 °C, the fragments generated in CMP caused surface damage, resulting in high surface roughness. The product calcined at 900 °C had a layered structure, and its chemical activity and mechanical hardness were matched the best; thus, it had the best polishing performance for K9.

The polishing mechanism of the hierarchical layered quasi-triangular CeO_2 is shown in Figure 11. The abrasive particles approach the workpiece surface and chemically and mechanically interact with the K9 surface under pressure. The substances removed from the workpiece surface are entrained in the layered structure of quasi-triangular CeO_2 and leave the K9 surface along with the particles. The abrasive particles shake off the substances entrained in the layer, exposing a fresh surface. The fresh particles approach the K9 surface, and the above process is repeated.

4. CONCLUSIONS

Layered quasi-triangular $Ce(OH)CO_3$ assembled from primary nanoparticles was synthesized by a solvothermal method, and its formation mechanism was related to the continuous oxidation of EG by CeO_2 generated in the reaction system at high temperature and high pressure. The as-prepared $Ce(OH)CO_3$ was transformed to CeO_2 abrasives by calcination at 800−1000 °C. The microstructure, mechanical hardness, and chemical activity of the obtained CeO_2 abrasives changed with the calcination temperature, thus affecting the polishing performance. With an increase in calcination temperature, the size of the primary particles increased. The products calcined at 800−900 °C kept the layered edge structure of $Ce(OH)CO_3$ precursor, while the layered edges disappeared in the samples calcined at 950 and 1000 °C due to the large-scale melting of primary particles. The polishing tests on K9 glass showed that, in the calcination temperature range of 800−900 °C, the increase in hardness of the hierarchical layered quasi-triangular CeO_2 resulted in an increase in MRR. The decrease in surface chemical activity of quasi-triangular CeO_2 and disappearance of layered edges led to a sharp decrease of MRR in the calcination temperature range of 950−1000 °C. The product calcined at 900 °C maintained a layered edge structure, and its chemical activity and mechanical hardness were optimally matched and thus had the highest MRR for K9 glass and best surface quality after polishing.

■ ASSOCIATED CONTENT

ⓢ Supporting Information

The Supporting Information is available free of charge at https://pubs.acs.org/doi/10.1021/acsomega.2c07682.

> HRTEM images of the calcined products, peak areas of individual peaks of Ce 3d for calcined products, and SEM images of the calcined products after polishing (PDF)

■ AUTHOR INFORMATION

Corresponding Authors

Jing Li − School of Chemistry and Chemical Engineering and Institute of Rare Earths, Nanchang University, Nanchang 330031, People's Republic of China; ⓞ orcid.org/0000-0001-8630-8265; Email: lijingbuaa@163.com

Yongxiu Li − School of Chemistry and Chemical Engineering and Institute of Rare Earths, Nanchang University, Nanchang 330031, People's Republic of China; Email: yxli@ncu.edu.cn

Authors

Rucheng He − *School of Chemistry and Chemical Engineering, Nanchang University, Nanchang 330031, People's Republic of China*

Guihua Guo − *School of Chemistry and Chemical Engineering, Nanchang University, Nanchang 330031, People's Republic of China*

Yao Li − *School of Chemistry and Chemical Engineering, Nanchang University, Nanchang 330031, People's Republic of China*

Yuanyuan Liao − *School of Chemistry and Chemical Engineering, Nanchang University, Nanchang 330031, People's Republic of China*

Complete contact information is available at:
https://pubs.acs.org/10.1021/acsomega.2c07682

Author Contributions

The manuscript was written through contributions of all authors. All authors have given approval to the final version of the manuscript.

Notes

The authors declare no competing financial interest.

■ REFERENCES

(1) Dong, H.; Du, S. R.; Zheng, X. Y.; Lyu, G. M.; Sun, L. D.; Li, L. D.; Zhang, P. Z.; Zhang, C.; Yan, C. H. Lanthanide Nanoparticles: From design toward bioimaging and therapy. *Chem. Rev.* **2015**, *115*, 10725−10815.

(2) Liang, S.; Wang, H.; Li, Y.; Qin, H.; Luo, Z.; Huang, B.; Zhao, X.; Zhao, C.; Chen, L. Rare-earth based nanomaterials and their composites as electrode materials for high performance super-capacitors: a review. *Sustain. Energy Fuels* **2020**, *4*, 3825−3847.

(3) Zhang, Y.; Zhao, S.; Feng, J.; Song, S.; Shi, W.; Wang, D.; Zhang, H. Unraveling the physical chemistry and materials science of CeO$_2$-based nanostructures. *Chem.* **2021**, *7*, 2022−2059.

(4) Zheng, B.; Fan, J.; Chen, B.; Qin, X.; Wang, J.; Wang, F.; Deng, R.; Liu, X. Rare-earth doping in nanostructured inorganic materials. *Chem. Rev.* **2022**, *122*, 5519−5603.

(5) Trovarelli, A.; Llorca, J. Ceria catalysts at nanoscale: How do crystal shapes shape catalysis? *ACS Catal.* **2017**, *7*, 4716−4735.

(6) Montini, T.; Melchionna, M.; Monai, M.; Fornasiero, P. Fundamentals and catalytic applications of CeO$_2$-based materials. *Chem. Rev.* **2016**, *116*, 5987−6041.

(7) Wu, K.; Sun, L. D.; Yan, C. H. Recent progress in well-controlled synthesis of ceria-based nanocatalysts towards enhanced catalytic performance. *Adv. Energy Mater.* **2016**, *6*, 1600501.

(8) Zhu, Y.; Chen, C.; Cheng, P.; Ma, J.; Yang, W.; Yang, W.; Peng, Y.; Huang, Y.; Zhang, S.; Seong, G. Recent advances in hydrothermal synthesis of facet-controlled CeO$_2$-based nanomaterials. *Dlaton Trans.* **2022**, *51*, 6506−6518.

(9) Seo, J. A review on chemical and mechanical phenomena at the wafer interface during chemical mechanical planarization. *J. Mater. Res.* **2021**, *36*, 235−257.

(10) Srinivasan, R.; Dandu, P. VR; Babu, S. V. Shallow trench isolation chemical mechanical planarization: A review. *ESC J. Solid State Sci. Technol.* **2015**, *4*, P5029−P5039.

(11) Krishnan, M.; Nalaskowski, J. W.; Cook, L. M. Chemical mechanical planarization: slurry chemistry, materials, and mechanisms. *Chem. Rev.* **2010**, *110*, 178−204.

(12) Raza, R.; Zhu, B.; Rafique, A.; Naqvi, M. R.; Lund, P. Functional ceria-based nanocomposites for advanced low-temperature (300−600°C) solid oxide fuel cell: A comprehensive review. *Mater. Today Energy* **2020**, *15*, 100373.

(13) Jaiswal, N.; Tanwar, K.; Suman, R.; Kumar, D.; Upadhyay, S.; Parkash, O. A brief review on ceria based solid electrolytes for solid oxide fuel cells. *J. Alloys Compd.* **2019**, *781*, 984−1005.

(14) Mahato, N.; Banerjee, A.; Gupta, A.; Omar, S.; Balani, K. Progress in material selection for solid oxide fuel cell technology: A review. *Prog. Mater. Sci.* **2015**, *72*, 141−337.

(15) Chavhan, M. P.; Lu, C.-H.; Som, S. Urea and surfactant assisted hydrothermal growth of ceria nanoparticles. *Colloids Surf., A* **2020**, *601*, 124944.

(16) Dang, F.; Kato, K.; Imai, H.; Wada, S.; Haneda, H.; Kuwabara, M. Characteristics of CeO$_2$ nanocubes and related polyhedra prepared by using a liquid-liquid interface. *Cryst. Growth Des.* **2010**, *10*, 4537−4541.

(17) Alhumaimess, M.; Aldosari, O.; Alshammari, H.; Kamel, M. M.; Betiha, M. A.; Hassan, H. M. A. Ionic liquid green synthesis of CeO$_2$ nanorods and nano-cubes: Investigation of the shape dependent on catalytic performance. *J. Mol. Liq.* **2019**, *279*, 649−656.

(18) Huang, Y. C.; Wu, S. H.; Hsiao, C. H.; Lee, A. T.; Huang, M. H. Mild synthesis of size-tunable CeO$_2$ octahedra for band gap variation. *Chem. Mater.* **2020**, *32*, 2631−2638.

(19) Shi, J.; Wang, H.; Liu, Y.; Ren, X.; Sun, H.; Lv, B. Rapid microwave-assisted hydrothermal synthesis of CeO$_2$ octahedra with mixed valence states and their catalytic activity for thermal decomposition of ammonium perchlorate. *Inorg. Chem. Front.* **2019**, *6*, 1735−1743.

(20) Zhang, B.; Yu, H.; Wang, J.; Wang, W.; Zhang, Q.; Zhang, H. Synthesis of CeO$_2$ nanoparticles with different morphologies and their properties as peroxidase mimic. *J. Am. Ceram. Soc.* **2018**, *102*, 2218−2227.

(21) Liu, Z.; Zheng, J.; Duan, L.; Zhu, Z. Biomass-assisted synthesis of CeO$_2$ nanorods for CO$_2$ photoreduction under visible light. *ACS Appl. Nano Mater.* **2021**, *4*, 4226−4237.

(22) Ji, Z.; Wang, X.; Zhang, H.; Lin, S.; Meng, H.; Sun, B.; George, S.; Xia, T.; Nel, A. E.; Zink, J. I. Designed synthesis of CeO$_2$ nanorods and nanowires for studying toxicological effects of high aspect ratio nanomaterials. *ACS Nano* **2012**, *6*, 5366−5380.

(23) Li, J.; Zhang, Z.; Tian, Z.; Zhou, X.; Zheng, Z.; Ma, Y.; Qu, Y. Low pressure induced porous nanorods of ceria with high reducibility and large oxygen storage capacity: synthesis and catalytic applications. *J. Mater. Chem. A* **2014**, *2*, 16459−16466.

(24) Li, J.; Wang, C.; Zhu, X.; Wu, T.; Tang, B.; Li, Y. Synthesis of hierarchical CeO$_2$ octahedrons with tunable size and the catalytic properties. *Mater. Lett.* **2019**, *240*, 73−76.

(25) Han, X.; Li, L.; Wang, C. Synthesis of monodisperse CeO$_2$ octahedra assembled by nano-sheets with exposed {001} facets and catalytic property. *CrystEngComm* **2012**, *14*, 1939−1941.

(26) Zhang, H.; Wang, W.; Zhang, B.; Li, H.; Zhang, Q. Controllable synthesis of spherical cerium oxide particles. *RSC Adv.* **2016**, *6*, 30956−30962.

(27) Gong, J.; Meng, F.; Fan, Z.; Li, H.; Du, Z. Template-free controlled hydrothermal synthesis for monodisperse flowerlike porous CeO$_2$ microspheres and their superior catalytic reduction of NO with NH$_3$. *J. Alloys Compd.* **2017**, *690*, 677−687.

(28) Feng, Z.; Zhang, M.; Ren, Q.; Mo, S.; Peng, R.; Yan, D.; Fu, M.; Chen, L.; Wu, J.; Ye, D. Design of 3-dimensionally self-assembled CeO$_2$ hierarchical nanosphere as high efficiency catalysts for toluene oxidation. *Chem. Eng. J.* **2019**, *369*, 18−25.

(29) Liu, W.; Feng, L.; Zhang, C.; Yang, H.; Guo, J.; Liu, X.; Zhang, X.; Yang, Y. A facile hydrothermal synthesis of 3D flowerlike CeO$_2$ via a cerium oxalate precursor. *J. Mater. Chem. A* **2013**, *1*, 6942−6948.

(30) Zhang, X.; Hou, F.; Yang, Y.; Wang, Y.; Liu, N.; Chen, D.; Yang, Y. A facile synthesis for cauliflower like CeO$_2$ catalysts from Ce-

BTC precursor and their catalytic performance for CO oxidation. *Appl. Surf. Sci.* **2017**, *423*, 771−779.

(31) Tu, P. H.; Le, D. N.; Dao, D. T.; Doan, T. C. D.; Dang, C. M. Fabrication of nano-catalyst ceria flower and catalyst characterization. *Adv. Nat. Sci.: Nanosci. Nanotechnol.* **2019**, *10*, 025010.

(32) Wei, J.; Yang, Z.; Yang, Y. Fabrication of three dimensional CeO_2 hierarchical structures: precursor template synthesis, formation mechanism and properties. *CrystEngComm* **2011**, *13*, 2418−2424.

(33) Peng, W.; Guan, C.; Li, S. Material removal mechanism of ceria particles with different sizes in glass polishing. *Opt. Eng.* **2014**, *53*, 035104.

(34) Sreeremya, T. S.; Prabhakaran, M.; Ghosh, S. Tailoring the surface properties of cerium oxide nanoabrasives through morphology control for glass CMP. *RSC Adv.* **2015**, *5*, 84056−84065.

(35) Hu, P.; Chen, Y.; Sun, R.; Chen, Y.; Yin, Y.; Wang, Z. Synthesis, characterization and frictional wear behavior of ceria hybrid architectures with {111} exposure planes. *Appl. Surf. Sci.* **2017**, *401*, 100−105.

(36) Kim, N. Y.; Kim, G.; Sun, H.; Hwang, U.; Kim, J.; Kwak, D.; Park, I. K.; Kim, T.; Suhr, J.; Nam, J. D. A nanoclustered ceria abrasives with low crystallinity and high Ce^{3+}/Ce^{4+} ratio for scratch reduction and high oxide removal rates in the chemical mechanical planarization. *J. Mater. Sci.* **2022**, *57*, 12318−12328.

(37) Liu, C.; Lin, Y. C.; Yoon, M.; Yu, Y.; Puretzky, A. A.; Rouleau, C. M.; Chisholm, M. F.; Xiao, K.; Eres, G.; Duscher, G.; Geohegan, D. B. Understanding substrate-guided assembly in van de Waals epitaxy by in situ laser crystallization within a transmission electron microscope. *ACS Nano* **2021**, *15*, 8638−8652.

(38) Hendrikse, H. C.; Weijden, A. V. D.; Ronda-Lloret, M.; Yang, T.; Bliem, R.; Shiju, N. R.; Hecke, M. V.; Li, L.; Noorduin, W. L. Shape-preserving chemical conversion of architected nanocomposites. *Adv. Mater.* **2020**, *32*, 2003999.

(39) Gao, K.; Zhu, Y. Y.; Tong, D. Q.; Tian, L.; Wang, Z. H.; Wang, X. Z. Hydrothermal synthesis of single-crystal $CeCO_3OH$ and their thermal conversion to CeO_2. *Chin. Chem. Lett.* **2014**, *25*, 383−386.

(40) He, L.; Li, J.; Feng, Z.; Sun, D.; Wang, T.; Li, R.; Xu, Y. Solvothermal synthesis and characterization of ceria with solid and hollow spherical and multilayered morphologies. *Appl. Surf. Sci.* **2014**, *322*, 147−154.

(41) Mao, X.; Xia, X.; Li, J.; Chen, C.; Gu, X.; Li, S.; Lan, Y. P. Self-assembly of structured $CeCO_3OH$ and its decomposition in H_2 for a novel tactic to obtained CeO_{2-x} with excellent photocatalytic property. *J. Alloys Compd.* **2021**, *870*, 159424.

(42) Ding, H.; Yang, J.; Ma, S.; Yigit, M.; Xu, J.; Rupprechter, G.; Wang, J. Large dimensional CeO_2 nanoflakes by microwave-assisted synthesis: lamellar nano-channels and surface oxygen vacancies promote catalytic activity. *Chem. Catal. Chem.* **2018**, *10*, 4100−4108.

(43) Huang, X.; Zhang, K.; Peng, B.; Wang, G.; Muhler, M.; Wang, F. Ceria-based materials for thermocatalytic and photocatalytic organic synthesis. *ACS Catal.* **2021**, *11*, 9618−9678.

(44) Xu, Y.; Wu, P.; Wu, M.; Gu, Y.; Yu, H.; Ding, Z. Solvothermal synthesis, structural characterization and optical properties of Pr-doped CeO_2 and their degradation for acid orange 7. *Mater.* **2022**, *15* (19), 6953.

(45) Gao, W.; Wei, Q.; Ding, L.; Li, X.; Wang, C.; Tang, G.; He, J. Electrokinetic research on the dispersion behavior of nano-ceria particles in concentrated suspensions. *Key Eng. Mater.* **2015**, *645−646*, 394−399.

(46) Cacua, K.; Ordonez, F.; Zapata, C.; Herrera, B.; Pabon, E.; Buitrago-Sierra, R. Surfactant concentration and pH effects on the zeta potential values of alumina nanofluids to inspect stability. *Colloids Surf., A* **2019**, *583*, 123960.

(47) Lawrence, N. J.; Brewer, J. R.; Wang, L.; Wu, T. S.; Wells-Kingsbury, J.; Ihrig, M. M.; Wang, G.; Soo, Y. L.; Mei, W. N.; Cheung, C. L. Defect engineering in cubic cerium oxide nanostructures for catalytic oxidation. *Nano Lett.* **2011**, *11*, 2666−2671.

(48) Maslakov, K. I.; Teterin, Y. A.; Popel, A. J.; Teterin, A. Y.; Ivanov, K. E.; Kalmykov, S. N.; Petrov, V. G.; Petrov, P. K.; Farnan, I.

XPS study of ion irradiated and unirradiated CeO_2 bulk and thin film samples. *Appl. Surf. Sci.* **2018**, *448*, 154−162.

(49) Sims, C. M.; Maier, R. A.; Johnston-Peck, A. C.; Gorham, J. M.; Hackley, V. A.; Nelson, B. C. Approaches for the quantitative analysis of oxidation state in cerium oxide nanomaterials. *Nanotechnology* **2019**, *30*, 085703.

(50) Seo, J.; Moon, J.; Kim, J. H.; Lee, K.; Hwang, J.; Yoon, H.; Yi, D. K.; Paik, U. Role of the oxidation state of cerium on the ceria surfaces for silicate adsorption. *Appl. Surf. Sci.* **2016**, *389*, 311−315.

(51) Choi, J.; Shin, C.; Yang, J.; Chae, S.; Kim, T. Effect of ceria abrasive synthesized by supercritical hydrothermal method for chemical mechanical planarization. *ESC J. Solid State Sci. Technol.* **2019**, *8*, P3128−P3132.

(52) Ma, W.; Mashimo, T.; Tamura, S.; Tokuda, M.; Yoda, S.; Tsushida, M.; Koinuma, M.; Kubota, A.; Isobe, H.; Yoshiasa, A. Cerium oxide (CeO_{2-x}) nanoparticles with high Ce^{3+} proportion synthesized by pulsed plasma in liquid. *Ceram. Int.* **2020**, *46*, 26502−26510.

(53) Netzband, C. M.; Dunn, K. Controlling the cerium oxidation state during silicon oxide CMP to improve material removal rate and roughness. *ESC J. Solid State Sci. Technol.* **2020**, *9*, 044001.

(54) Cook, L. M. Chemical process in glass polishing. *J. Non-Cryst. Solids* **1990**, *120*, 152−171.

(55) Hoshino, T.; Kurata, Y.; Terasaki, Y.; Susa, K. Mechanism of polishing of SiO_2 films by CeO_2 particles. *J. Non-Cryst. Solids* **2001**, *283*, 129−136.

(56) Wang, Y. G.; Zhang, L. C.; Biddut, A. Chemical effect on the material removal rate in the CMP of silicon wafers. *Wear* **2011**, *270*, 312−316.

(57) Sahir, S.; Yerriboina, N. P.; Han, S. Y.; Han, K. M.; Kim, T. G.; Mahadev, N.; Park, J. G. Investigation of the effect of different cleaning forces on Ce-O-Si bonding during oxide post-CMP cleaning. *Appl. Surf. Sci.* **2021**, *545*, 149035.

(58) Dawkins, K.; Rudyk, B. W.; Xu, Z.; Cadien, K. The pH-dependent attachment of ceria nanoparticles to silica using surface analytical techniques. *Appl. Surf. Sci.* **2015**, *345*, 249−255.

(59) Dandu, P. V.; Peethala, B.; Babu, S. Role of different additives on silicon dioxide film removal rate during chemical mechanical polishing using ceria-based dispersion. *J. Electrochem. Soc.* **2010**, *157*, H869.

(60) Kim, K.; Seo, J.; Lee, M.; Moon, J.; Lee, K.; Yi, D. K.; Paik, U. Ce^{3+}-enriched core-shell ceria nanoparticles for silicate adsorption. *J. Mater. Res.* **2017**, *32*, 2829−2836.